PHYSICAL REVIEW E

STATISTICAL PHYSICS, PLASMAS, FLUIDS, AND RELATED INTERDISCIPLINARY TOPICS

THIRD SERIES, VOLUME 60, NUMBER 5 PART B NOVEMBER 1999

ARTICLES

Drying of capillary porous media with a stabilized front in two dimensions

M. Prat* and F. Bouleux

Institut de Mécanique des Fluides de Toulouse, UMR CNRS–INP/UPS No. 5502, Avenue du Professeur Camille Soula, 31400 Toulouse, France

(Received 26 April 1999)

We study a two-dimensional model of drying of capillary porous media when gravity or viscous forces lead to the formation of a stabilized front. When gravity forces stabilize the front, the mean front width, defined as the mean perpendicular distance between the front's most advanced and least advanced points, is found theoretically to scale with the Bond number B as $B^{-1+(1+\beta)/(1+\nu)}$, where β is the percolation probability exponent and ν is the correlation length exponent. This scaling is confirmed numerically and is consistent with the experimental results of Shaw [Phys. Rev. Lett. **59**, 1671 (1987)]. The global mass transfer coefficient of the front is studied numerically. To this end, we study the position $z_c-\delta$ of the equivalent smooth line leading to the same evaporation flux as the front. In the transient case, $z_c-\delta$ is found to scale with the Bond number B as $B^{-0.63}$. In the stationary case, i.e., when the front reaches a stationary position within the medium, it is found that $z_c-\delta\approx\sigma$ where σ is the standard deviation of the positions of the points forming the front around its mean position z_c. These results are exploited to study the evaporation flux when viscous effects stabilize the front. In particular, we discuss the possibility of nontrivial behaviors, i.e., drying rates not scaling as $1/\sqrt{t}$ for drying under constant external conditions. [S1063-651X(99)06811-7]

PACS number(s): 47.55.Mh, 64.60.Ak, 64.70.Fx

I. INTRODUCTION

Drying of capillary porous media has been the object of a large number of studies [1–4], and references therein, since the pioneering work of Ceaglske and Hougen [5]. Most of these have been conducted within the framework of the continuum approach to porous media. More recently, [6–8], it has been shown that drying could be also studied within the framework of the discrete approach [9]. In this context, it turns out that invasion percolation (IP) concepts can be used to analyze slow drying. Invasion percolation models have been used extensively to study slow drainage in porous media [10,11], and as, at least at first glance, drying can be viewed as an invasion of the materials by gas, the relevance of invasion percolation concepts in drying is *a priori* not surprising. However, there are important differences between drainage and drying due to the additional effect of mass transfer in the gas phase in drying. As a result, there are original features in drying that are worth analyzing as a special class of IP process. As explained in Ref. [8], the phase distribution patterns, and thereby the drying rates, depend on the interplay between the capillary, gravity, and viscous forces. When gravity or viscous forces are not negligible, one obtains phase distributions that can be analyzed in terms of invasion percolation in a gradient (IPG) [12–14], i.e., IP in a field where the percolation probability p has a spatial gradient. As discussed in Ref. [11], one can distinguish two main IPG patterns depending on whether invasion is in a stabilizing gradient (IPSG) or a destabilizing gradient (IPDG), respectively. In drying, there is a number of situations that leads to IPDG patterns. For instance, surface tension gradients induced by composition or temperature gradients can lead to IPDG patterns, [15]. As in drainage, [14,16] gravity effects can lead to IPDG as well as IPSG patterns depending on the fluid density ratio and the main direction of the invasion with respect to the gravity vector direction, [8]. As explained below, viscous effects lead only to IPSG patterns in drying. In this paper, we concentrate on IPSG situations induced by stabilizing gravity or viscous effects. These situations are characterized by the formation of stable fronts. In this context, the main objectives of this paper are, first, to characterize the front width and the front global mass transfer coefficient. Then it is shown how these elements can

*Electronic address: prat@imft.fr

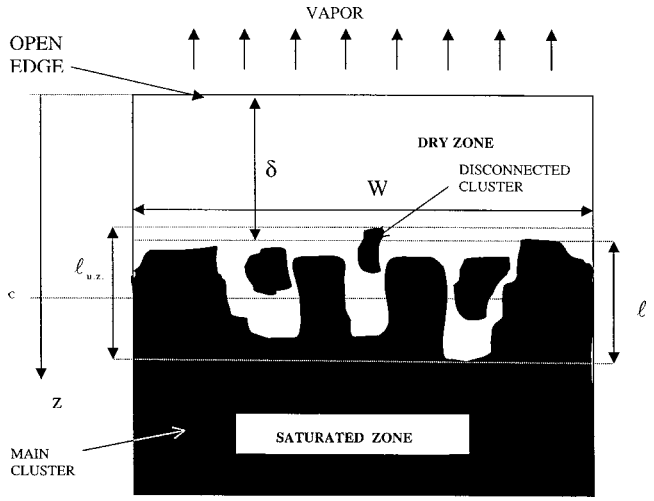

FIG. 1. Sketch of the situation studied.

be used to predict the drying rates. Transient situations, characterized by traveling fronts, as well as stationary situations are studied. The scaling law derived for the overall front width holds in two dimensions, and most of the other results reported here are based essentially on numerical simulations on a two-dimensional (2D) square lattice and therefore are pertinent only for 2D cases. This is certainly a limitation of the present study, that can be considered as a first step toward the full study of drying within the discrete approach framework. It should be noted, however, that there exist 2D systems of practical importance. Fractures and static seals are just two examples of such systems. Also, as in several previous studies [6–8], we consider the simplest drying situation in which thermal effects can be disregarded. The wetting fluid is the liquid that evaporates. The effects of liquid films that can carpet the pore walls after an invasion of the pore bulk by the gas phase are ignored. The liquid films may, however, significantly affect the drying rates under certain circumstances (pores and throats with corners or marked roughness inducing secondary capillary effects) [17]. The system investigated is depicted in Fig. 1. There is a net evaporation mass transfer from the interstitial liquid-gas interfaces toward the bulk gas surrounding the porous medium. The liquid phase is assumed to consist of a single component liquid, so that additional complications due to liquid composition variations can be ignored. The gas phase is a binary mixture consisting of the vapor of the liquid, component *A*, and an inert component, component *B*. The total pressure of the gas mixture is assumed to be constant. The mass transfer process in the gas phase is therefore determined by the binary diffusion of *A*. As thermal effects are negligible, the equilibrium concentration, denoted by c_e, of component *A* at the liquid-gas interfaces remains constant. This is a consequence of the simplifying assumption that the curvature of the interface is sufficiently large so that the Kelvin effect is neglected. We also assume that the density of the gas phase is negligible compared to the liquid density. Finally, we consider the case where the porous medium is initially completely saturated by liquid.

II. PHASE DISTRIBUTIONS

In this section we briefly discuss the various structures of the phase distributions that can be expected depending on the relative influence of the capillary, gravity, and viscous forces. As explained above, the analysis is restricted to IP and IPSG situations. In this section, we make use of macroscopic concepts, while in Sec. V, using IP concepts and results presented in this paper, a more refined study is presented for 2D geometries. The idea is to compare the size L of the porous medium sample (Fig. 1) to a characteristic length L_g of a gravity front and to a characteristic length L_{cap} of a viscous front. L_g represents the distance over which the pressure difference δP_h, due to gravity, becomes comparable to the pressure jump P_c at a meniscus due to capillarity. This can be expressed as

$$\delta P_h = \rho_L L_g g = P_c \approx \frac{2\gamma\cos\theta}{\overline{r}}, \tag{1}$$

where γ is the surface tension, θ the wetting angle, and $\overline{r}$ is an average pore size. ρ_L is the liquid density, and g the acceleration of gravity. Therefore,

$$\frac{L_g}{\overline{r}} \approx B^{-1}, \tag{2}$$

where B is the Bond number, defined here as $B^{-1} = 2\gamma\cos\theta/\overline{r}^2\rho_L g$ (the Bond number describes the relative importance of gravity over capillary forces). L_{cap} represents the distance over which the pressure difference due to viscous effects becomes comparable to P_c. If k is the porous medium permeability, one can express L_{cap} as [8]

$$\frac{L_{\mathrm{cap}}}{\overline{r}} \approx \frac{k}{\overline{r}^2}\mathrm{Ca}^{-1}, \tag{3}$$

where the capillary number Ca, which characterizes the competition between the viscous and the capillary forces, is defined by $\mathrm{Ca}^{-1} = 2\gamma\cos\theta/\mu_L v$, where v is a characteristic liquid filtration velocity and μ_L is the liquid dynamic viscosity. One problem is to define v. Another is to take into account the fact that v diminishes during the process. Here we identify v with the filtration velocity at the onset of the process. Under these circumstances, one may define v as

$$v = e/\rho_L, \tag{4}$$

where e is the evaporation flux density. As under standard constant external drying conditions e decreases during the process, L_{cap} progressively increases. Therefore, in some cases, one may have $L_{\mathrm{cap}} < L$, and therefore a viscous front at the beginning of the process, whereas later L_{cap} may become larger than L, which corresponds to a capillarity-dominated regime.

III. GRAVITY STABILIZED DRYING FRONTS

A. Overall front width

The structure of drainage fronts stabilized by gravity was first studied by Wilkinson [18], and subsequently in several papers [12,14]. These works confirmed the main results of Wilkinson. First, the structure of the front is significantly different in two and three dimensions (see Ref. [13] for the 3D case). In two-dimensions, the front width σ can be defined by

$$\sigma^2=\frac{\int_0^\infty (z_c-z)^2 p_f(z)dz}{\int_0^\infty p_f(z)dz},$$

where z_c is the mean position of the front,

$$z_c=\frac{\int_0^\infty z p_f(z)dz}{\int_0^\infty p_f(z)dz},$$

and $p_f(z)$ is the probability of finding one site of the front at z. As discussed, for instance, in Ref. [14], it is found that the front width σ scales as

$$\sigma \propto B^{-\nu/(1+\nu)}, \tag{5}$$

where ν is the correlation length exponent. This leads to $\sigma \propto B^{-0.57}$ in two-dimensions. This length scale in fact characterizes the width of the fractal region of the front around the mean front position z_c. It is also of interest to consider the overall extent of the front, which is the perpendicular distance between the front most advanced and least advanced points. More precisely, we are interested in the mean value of this distance (the overall extent itself is a stochastic variable whose standard deviation is decreasing to zero with the ratio of front width to lattice size). This mean width is noted hereafter by l. l corresponds in fact to the width of the transition zone discussed in Ref. [18]. Using arguments similar to the ones used for obtaining Eq. (2), Wilkinson showed that the width of this zone should scale as B^{-1}. To derive this scaling, he assumed that the capillary pressure at the top and at the bottom of the transition zone was independent of B. This assumption is not valid in two dimensions. In what follows, the correct 2D scaling is derived. We start from the following relation first derived by Wilkinson [18], and extended here by taking into account the influence of the width of the bond size distribution

$$S_w^*-S_w \propto \left(\frac{B}{\Sigma}\right)^{(1+\beta)/(1+\nu)}, \tag{6}$$

in which B is the Bond number, S_w^* the wetting fluid residual saturation for $B=0$, and S_w the residual saturation at finite Bond number. β is the percolation probability exponent (for simplicity, we assume a uniform bond width distribution in the range $[r_{\min},r_{\max}]$ with $\Sigma=(r_{\max}-r_{\min})/a$, where a is the lattice spacing). If q is the fraction of the bond that is occupied by the wetting fluid at the residual saturation, Eq. (6) indicates that

$$q^*-q \propto \left(\frac{B}{\Sigma}\right)^{(1+\beta)/(1+\nu)}. \tag{7}$$

In terms of the fraction p of the bond occupied by the nonwetting fluid, one therefore has

$$p-p^* \propto \left(\frac{B}{\Sigma}\right)^{(1+\beta)/(1+\nu)}. \tag{8}$$

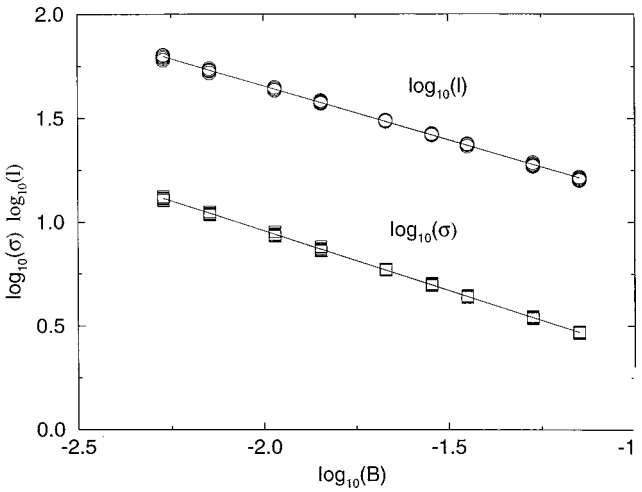

FIG. 2. Front width σ and front width l as a function of the Bond number. The slopes of the straight lines are -0.5738 ± 0.0017 for σ and -0.5187 ± 0.0025 for l, in excellent agreement with the theory. These results were obtained with square lattices of size 400×400.

As mentioned above, a uniform bond width distribution in the range $[r_{\min},r_{\max}]$ is assumed, hence $p=[(r_{\max}-r)/a\Sigma]$. In terms of bond width, one has, consequently,

$$r^*-r \propto \Sigma\left(\frac{B}{\Sigma}\right)^{(1+\beta)/(1+\nu)}. \tag{9}$$

In the equation above, r can be viewed as the size of the narrowest bonds that are invaded. It is well known that in the absence of gravity forces the invasion percolation process leads to invasion of bonds in the range $[r_c-r_{\max}]$, where r_c corresponds to the lattice percolation threshold p_c. In the presence of gravity forces, Eq. (9) indicates that the lower bound of the invaded bond sizes decreases as B increases. This also indicates that in fact $r^*=r_c$. As the total width of the front (defined as the perpendicular distance between the front most advanced and least advanced points) is determined from the equilibrium between the capillary forces and the gravity forces, one deduces (we know from Ref. [19] that the mean position of the front corresponds to r_c)

$$l \approx 2B^{-1}(r^{-1}-r_c^{-1}). \tag{10}$$

Then a Taylor expansion of r^{-1} leads to

$$l \approx 2B^{-1}\frac{(r_c-r)}{r_c^2}. \tag{11}$$

Taking into account Eq. (9), one finally obtains

$$l \propto \frac{2}{r_c^2}\left(\frac{B}{\Sigma}\right)^{-1+[(1+\beta)/(1+\nu)]}. \tag{12}$$

This scaling has been checked numerically. Using the standard invasion percolation algorithm and the invasion potential defined for taking into account stabilizing gravity forces [7,8], simulations were performed for six realization of a square 400×400 network. For each realization, the mean front thicknesses σ and l were determined for 12 different

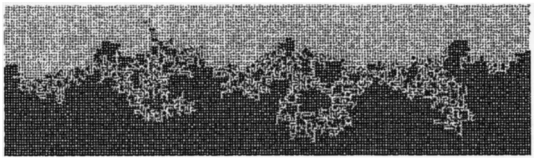

FIG. 3. Numerical simulation of a stabilized drying front on a square lattice of size 200×200. The liquid phase is in black, the gas phase in light gray. Note the disconnected clusters.

values of the Bond number, while Σ was kept constant. The results are shown in Fig. 2. The slopes reported in Fig. 2 are in excellent agreement with the expected scaling for σ, i.e., -0.57, and the scaling given by Eq. (12), i.e., -0.52. The influence of the width of the bond distribution Σ was also checked by varying Σ for a given Bond number and the results (not reported in this paper) are in excellent agreement with the theoretical predictions (the fact that increasing Σ has an effect which is equivalent to an increase in capillarity was mentioned in Ref. [11]).

B. Transient case

In the transient case, the mass transfer between the porous medium and its surroundings takes place only through the top side of system. The bottom and lateral sides are impervious. A typical phase distribution for this case is shown in Fig. 3. Note the disconnected liquid clusters in the front region. The phase distribution depicted in Fig. 3 was obtained by means of a pore network simulation based on the drying model proposed in Ref. [7], and subsequently validated by comparison with experiments as reported in Ref. [8]. This pore network drying simulator, which was described in several papers (cf. Refs. [7] and [8]) can be summarized as follows: (1) every cluster present in the network [a square lattice of sites (pores) and bonds (throats) of random width was used] is identified; (2) the bond connected to the already invaded region which has the lowest invasion potential is identified for each cluster; (3) the evaporation flux at the boundary of each cluster is computed; (4) for each cluster, the mass loss corresponding to the evaporation flux determined in step (3) is assigned to the bond identified in step (2); (5) the bond (as well as the adjacent pore) eventually invaded is that which is the first to be completely drained among the bonds selected in step (2); and (6) the phase distribution within the network is updated. The evaporation flux [step (3)] is determined from the computation of the molar fractions in the vapor phase. The invasion potential mentioned in step (2) is defined as the difference between the threshold capillary pressure of the bond and the pressure difference across the meniscus located in that bond, i.e., $Q(l,z)=(2\gamma/r_l)-[P_g-P_l(z)]$ where r_l is the radius of the bond (throughout this paper a perfectly wetting liquid is assumed). The total pressure in the gas phase P_g is assumed to be constant, while the liquid pressure (P_l) distribution remains hydrostatic. As indicated above, vapor was allowed to escape through the top edge of network. Zero flux conditions were imposed on the three remaining edges. This simulator was used to study the average properties of the front.

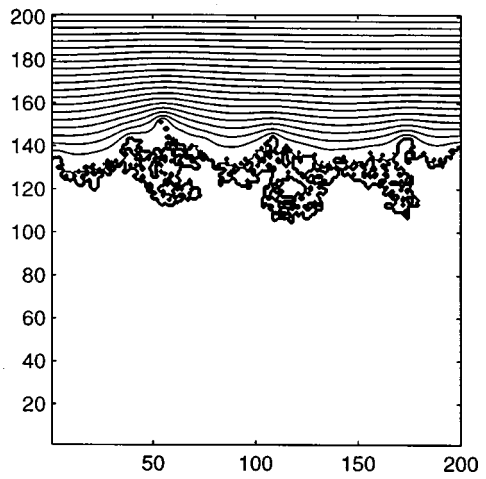

FIG. 4. Example of vapor concentration distribution in the gas phase (the front is the one depicted in Fig. 3).

1. Front global mass transfer coefficient

The objective is to characterize the average mass transfer by molecular diffusion between the front region and the top edge of network. Generally in drying, the external transfer resistance becomes negligible compared to the transfer resistance within the materials once a dry zone is created within the medium. Here, for simplicity, we consider a negligible external transfer resistance, i.e., $c\approx 0$ at $z=0$ when there is a dry zone. During the period between two pore invasions, the vapor concentration field in the gas phase within the porous medium corresponds to the quasisteady solution with the equilibrium concentration imposed at each meniscus. This is due to the fact that the typical time scale of diffusion over a distance of the order a pore length is very short compared to the overall duration of the drying process. Figure 4 shows the typical structure of the vapor concentration field in the gas phase in our problem. The isoconcentration lines become flat and unperturbed sufficiently away from the front region. This type of situation was considered in detail in Ref. [20] for self-affine interfaces. The global mass transfer coefficient was evaluated by studying the position of the equivalent smooth boundary leading to the same unperturbed far field as for the self-affine interface. By employing the same concept, we studied the position δ of the smooth line at uniform concentration c_e leading to the same concentration field in the far field as for the drying front. Practically this means that, if one is interested only in the evaporation flux, one could replace the irregular front by a straight line at concentration c_e. More precisely we have studied the position of this line with respect to the mean position of the front z_c, i.e., $\delta - z_c$. This amounts to define the global mass transfer coefficient Y of the front as

$$\Phi = Y c_e = \rho_v D^* b W \frac{c_e}{\delta}, \tag{13}$$

where ρ_v is the gas phase density, b is the thickness of the porous medium and W its width, Φ is the evaporation flux, and D^* is the effective diffusivity coefficient of the porous medium as defined in standard continuum models.

In order to make use of Eq. (13), D^* must be computed through pore network simulation. For the considered net-

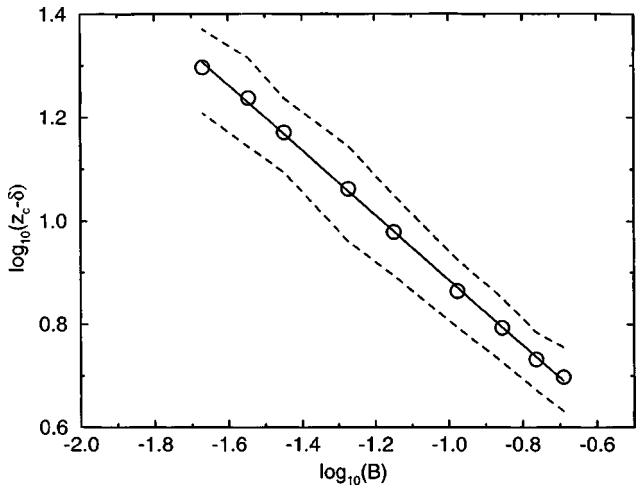

FIG. 5. Position of the equivalent smooth line as a function of the Bond number. The slope of the straight line is 0.230 ± 0.009. The dashed lines represent ± 1 standard deviations of $z_c - \delta$ obtained in numerical simulations. These results were obtained with square lattices of size 200×200.

work we found $D^* = 0.21D$ where D is the binary molecular diffusion coefficient for the gas mixture. Insight into the average behavior of the system is obtained from pore network simulations for 50 realizations of a 200×200 network. It should be noted that it becomes rapidly very tedious to use networks larger than 200×200 because of the concentration field computation that requires the solution of a linear system after each invasion (we used a conjugate gradient method on a workstation). For each realization, nine values of the Bond numbers were considered. We have first checked that the correct scaling for l and σ with the Bond number was obtained with this series of front. We found $-1+[(1+\beta)/(1+\nu)] = -0.514 \pm 0.008$ and $\nu/(1+\nu) = 0.573 \pm 0.009$, which are in very good agreement with the expected values (0.52 and 0.57, respectively). The theoretical prediction of the scaling of Y is not straightforward here because of the presence of the disconnected clusters. We know from the

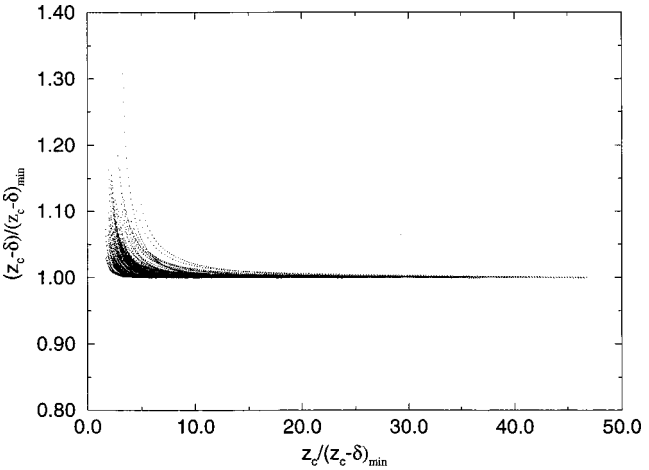

FIG. 6. Evolution of $z_c - \delta$ as a function of z_c. The results of ten realizations are plotted (nine different values of the Bond number were considered for each realization). $z_c - \delta$ reaches its established value when z_c is about equal to $10 \times (z_c - \delta)$. These results were obtained with square lattices of size 200×200.

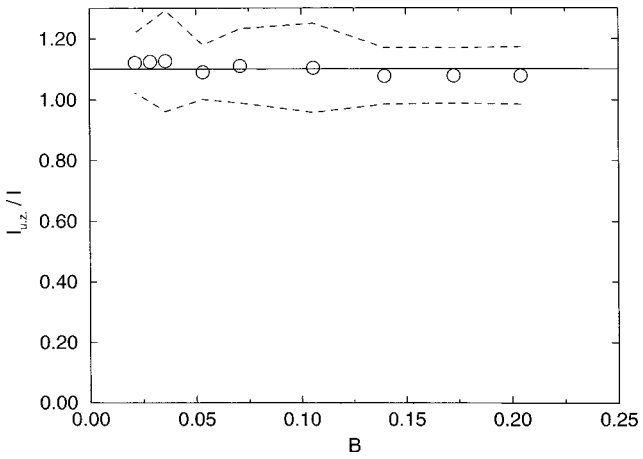

FIG. 7. Evolution of $l_{u.z.}/l$ as a function of the Bond number. Each symbol (○) corresponds to the average value of $l_{u.z.}/l$ over 50 realizations. The dashed lines represent ± 1 standard deviations of $l_{u.z.}/l$ obtained in numerical simulations. These results were obtained with square lattices of size 200×200.

work of Wilkinson [18], that the maximum size $L_{\max}$ of the clusters decreases with the bond number as $L_{\max} \propto B^{-\nu/(1+\nu)}$. We also know that many menisci are not active in terms of evaporation. Only the menisci located at the external boundary of the transition zone are active. Although it would therefore probably be interesting to study the statistical properties of the rough interface corresponding to the active menisci as a function of the Bond number, here we simply tried to correlate the evolution of Y (or, equivalently, $z_c - \delta$) to the Bond number variations. Not surprisingly, we obtained that $\sigma < (z_c - \delta) < l/2$. Regarding the Bond number dependence, we found, as shown in Fig. 5, that

$$(z_c - \delta) = m \left(\frac{B}{\Sigma} \right)^{-\lambda}, \tag{14}$$

with $\lambda = 0.628 \pm 0.007$, and where m is a numerical prefactor. This scaling corresponds to the drying period during which the front is established as explained below.

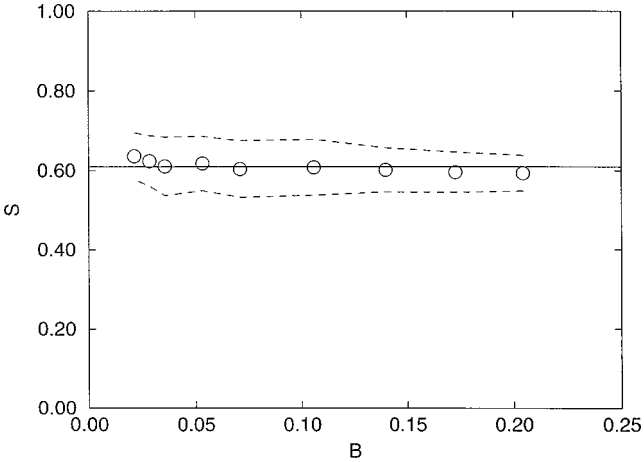

FIG. 8. Front overall saturation S as a function of B. Each symbol (○) corresponds to the average value of S over 50 realizations. The dashed lines represent ± 1 standard deviations of S obtained in numerical simulations. These results were obtained with square lattices of size 200×200.

2. Average drying rates

We are now in a position to model the average drying rates. Two phases may be distinguished: (1) an initial phase before the establishment of the front, and (2) a second phase when the front is established and Y reaches a constant value. As shown in Fig. 6, the second phase is reached approximately when $z_c \approx 10(z_c - \delta)$. Hereafter, we consider the second phase. For a given Bond number, the overall saturation S of the transition zone, i.e., the average saturation in the region included between the most advanced point of the front most and least advanced points of the liquid distribution is a constant (due to disconnected clusters, this region may be *a priori* expected to be slightly larger than the front width l. If $l_{u.z.}$ is the width of this region, defined as the perpendicular distance between the most advanced point of the front and the least advanced point of the liquid distribution, the simulations indicates that $l_{u.z.}/l \approx 1.1$ regardless of the Bond number value as reported in Fig. 7). As a matter of fact, the simulations indicate a weak dependence of S with B as shown in Fig. 8. Throughout this paper, variations of S with B, if any, are ignored. The mass balance for the traveling front can be expressed as

$$\rho_L \varepsilon S W b \frac{dz_c}{dt} = \Phi, \tag{15}$$

where ε is the porosity of the porous medium. Taking into account Eqs. (13) and (14), this leads to the equation

$$0.5 z_c^2 - m\left(\frac{B}{\Sigma}\right)^{-\lambda} z_c + C = \frac{\rho_v D^* c_e}{\varepsilon S \rho_L} t, \tag{16}$$

where C is a constant [at $t=0$, one should have $z_c \approx 10(z_c - \delta)$]. This leads to the classic behavior $\Phi \propto t^{-1/2}$ since in fact as $m(B/\Sigma)^{-\lambda}$ is $O(l)$ and $z_c > 10(z_c - \delta)$ (front established) the second term on the left hand side of Eq. (16) is negligible.

IV. VISCOSITY STABILIZED DRYING FRONTS

A. Transient case

1. Shaw's experiment

To the best of our knowledge, Shaw [6] was the first to study drying within the framework of percolation when viscous effects are important. He showed that viscous effects lead to the formation of a stable traveling fractal front. If we note that in drying the displacing phase (gas) is less viscous than the displaced phase (liquid), then in a direct analogy with the corresponding drainage pattern we would expect not a stable front but viscous fingering (see Ref. [21]). In drying, however, the average velocity in the liquid tends to be directed toward the inlet (and not toward the outlet as in drainage). As a result, the pressure gradients stabilize the front similarly to the way hydrostatic pressure gradients induced by gravity lead to a stabilized invasion front. Therefore, IPG can be used to determine the behavior of the front width σ as a function of the capillary number $\mathrm{Ca} = \nu\mu/\gamma$. In drainage, Wilkinson [18] obtained that σ scales as $\mathrm{Ca}^{-\nu/(t-\beta+1+\nu)}$ where t, β, and ν are the conductivity, percolation-probability, and correlation length exponents, respectively.

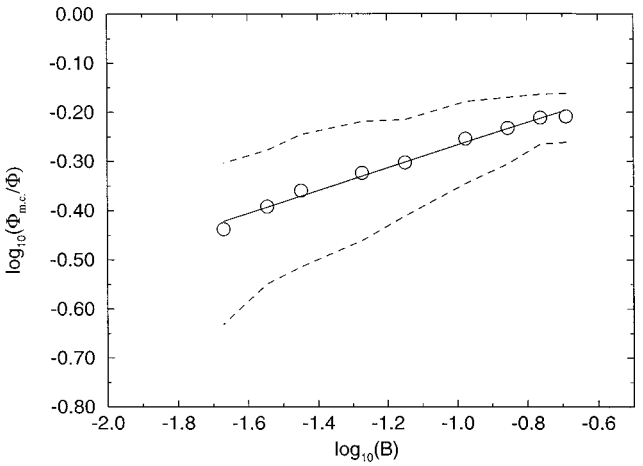

FIG. 9. Evolution of the fractional evaporation flux $f = \Phi_{\mathrm{m.c.}}/\Phi$ as a function of the Bond number. Each symbol (○) corresponds to the average value of f over 50 realizations. The dashed lines represent ± 1 standard deviations of f obtained in numerical simulations. These results were obtained with square lattices of size 200×200.

In drying, however, there is no pressure gradient in the displacing phase. As discussed by Shaw [6], this leads to a different scaling, i.e., $\sigma \propto \mathrm{Ca}^{-\nu/(1+\nu)}$. Shaw [6] conducted two-dimensional experiments with packings of very small spheres (0.5-μm diameter), and found an exponent of -0.48 ± 0.1 which despite the scatter in the experimental data was significantly lower than the theoretical prediction $-\nu/(1+\nu) = -0.57$ in two dimensions. Shaw [6], however, used the overall front width l as defined in Sec. III A, and not σ, to characterize the front width. He assumed that the scaling for the overall front width was the same as for σ, i.e., $\mathrm{Ca}^{-\nu/(1+\nu)}$. From the result of Sec. III A, the correct scaling is in fact $l \propto \mathrm{Ca}^{-1(1+\beta)/(1+\nu)}$. This gives a value of -0.52 in two dimensions, instead of -0.57, which is significantly closer to the experimental value (-0.48) determined by Shaw. Although the theoretical prediction is now closer to the experimental value, the theoretical exponent of -0.52 is still somewhat larger than the exponent of -0.48 found by Shaw. As stated by Shaw, this may be due to possible pressure gradient variations across the width of the front. This issue is discussed further in Sec. V. It may be also put forward that the porous medium used by Shaw is not strictly 2D. The images presented in Shaw's paper are, however, typical of 2D invasions and therefore, we conclude that 3D effects, if any, are most probably negligible.

2. Drying rates

One interesting feature of viscous fronts under constant external transfer condition is that their extent increases as the front moves within the materials. This may be expected to lead to nontrivial behavior of the drying rates, i.e., drying rates not scaling with the time as $1/\sqrt{t}$. In order to develop some predictions regarding the drying rate, we must first address the problem of the reference velocity in the liquid. As mentioned above, our idea is to consider that the pressure gradient induced by the viscous forces in the liquid plays a role analogous to the hydrostatic pressure gradient (when gravity effects control the extent of the front). This leads

naturally to a consideration of scaling identical to that obtained for the gravity case, but where the capillary number replaces the Bond number [18]. An obvious candidate is the average evaporation velocity $v_e=\Phi/(\rho_L Wb)$. However, if one considers the fact that the evaporation is due, on the one hand, to the evaporation at the boundary of the disconnected clusters and, on the other hand, to the evaporation at the boundary of the main cluster, it is physically more appealing to consider $v_D=\Phi_{\mathrm{m.c.}}/(\rho_L Wb)$ as a reference velocity, where $\Phi_{\mathrm{m.c.}}$ is the evaporation flux at the boundary of the main cluster. We must now consider how the fractional flux $f=\Phi_{\mathrm{m.c.}}/\Phi$ scales as a function of Ca. The behavior found on the basis of the numerical simulations is shown in Fig. 9. It can be expressed as

$$f\propto B^{\chi}, \tag{17}$$

with $\chi=0.230\pm0.009$. Therefore, in the case of a viscous front we expect

$$f=n\left(\frac{\mathrm{Ca}}{\Sigma}\right)^{\chi}, \tag{18}$$

with $\mathrm{Ca}=v_D\mu_L/\gamma$, and n is a numerical prefactor.

We are now in a position to determine the evolution of the drying rates. A mass balance leads to the following equation:

$$-[1.1(S-1)+0.6]\frac{dl}{dt}+\frac{dz_c}{dt}=\frac{\rho_v D^* c_e}{\rho_L \varepsilon \delta}. \tag{19}$$

Using a^2/D^* as reference time, and a as a reference length, Eq. (19) can be written

$$-[1.1(S-1)+0.6]\frac{dl}{dt}+\frac{dz_c}{dt}=M\delta^{-1}, \tag{20}$$

where l, z_c, δ, and t are now dimensionless and $M=\rho_v c_e/\rho_L\varepsilon$.

Combining the Eqs. (18)–(20) leads to the following equation for δ:

$$\delta\frac{d\delta}{dt}-[1.1(S-1)+0.6]\left[\frac{n'\alpha N^{\alpha/(\chi-1)}}{1-\chi}\right]\delta^{\alpha/(1-\chi)}\frac{d\delta}{dt}+\left[\frac{m'\lambda N^{\lambda/(\chi-1)}}{1-\chi}\right]\delta^{\lambda/(1-\chi)}\frac{d\delta}{dt}=M, \tag{21}$$

where $N=n\rho_v D^* c_e\mu_L/a\Sigma\gamma$. In Eq. (21), n' and m' are the numerical prefactors corresponding to the scaling of $z_c-\delta$ and l, i.e. $z_c-\delta=m'(\mathrm{Ca}/\Sigma)^{-\lambda}$ and $l=n'(\mathrm{Ca}/\Sigma)^{-\alpha}$, with $\alpha=1-[(1+\beta)/(1+\nu)]=0.52$. Finally, the evolution of δ as a function of time can be determined by solving the equation

$$0.5\delta^2-[1.1(S-1)+0.6]\times\left[\frac{n'\alpha N^{\alpha/(\chi-1)}}{[1+\alpha/(1-\chi)](1-\chi)}\right]\delta^{\alpha/(1-\chi)+1}+\left[\frac{m'\lambda N^{\lambda/(\chi-1)}}{[1+\lambda/(1-\chi)](1-\chi)}\right]\delta^{\lambda/(1-\chi)+1}=M(t-t_0)+C, \tag{22}$$

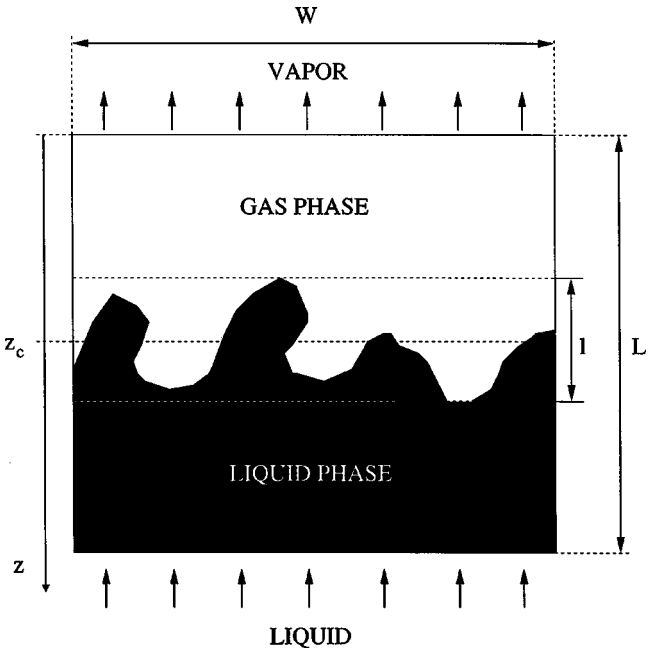

FIG. 10. Sketch of the stationary case.

where $[\alpha/(1-\chi)]+1\approx1.7$ and $[\lambda/(1-\chi)]+1\approx1.8$. t_0 is the time associated with the establishment of the front. C is a constant [for $t=t_0$, we must have $z_c\approx10(z_c-\delta)$ according to Fig. 6]. With these values for the exponents, Eq. (22) indicates that the first term on the left-hand side of Eq. (22) dominates for long times. In this case, a classical behavior is obtained, i.e., drying rates scale as $1/\sqrt{t}$. One interesting problem is to determine the influence of the second and third terms on the left-hand side of Eq. (22) before the first one starts to dominate. To explore this issue, we must first recall that Eq. (22) is valid only for the established front, i.e., when $z_c\geqslant10(z_c-\delta)$. Assuming a negligible external transfer resistance, it is not difficult to show that the position of the equivalent smooth line δ_c for which we have $z_c=10(z_c-\delta_c)$ is $\delta_c=(10m'N^{-\lambda/(1-\chi)})[(1-\chi)/(1-\chi-\lambda)]$. Substituting this expression for δ into Eq. (22) shows that the third term depends only on the values of the exponents and the factor 10 in the relation $z_c=10(z_c-\delta_c)$. With the values found for the exponents, it is obtained that the third term is about ten times smaller that the first one for $\delta=\delta_c$. The magnitude of the second term depends on the exponents, the prefactors n', m', and N, which depends on the fluid considered and on the lattice spacing. If we use the values of the prefactors deduced from our numerical simulations and consider, for instance, a porous medium saturated by water for ordinary laboratory conditions ($T\approx20\,^{\circ}\mathrm{C}$) and pore size in the usual range ($a\approx10^{-3}-1$ mm), we can conclude that the second term is negligible compared to the two other terms. Therefore, one concludes that in fact the drying essentially proceeds with the $1/\sqrt{t}$ law when Eq. (22) holds [note that the exponent of the third term on the left-hand side of Eq. (22) is relatively close to $2([\lambda/(1-\chi)]+1\approx1.8)$]. It should be noted, however, that it is possible to have a viscosity-controlled expanding front in a porous sample without reaching the regime associated with Eq. (22). For instance, for a lattice spacing $a=10\,\mu$m and water at 20 °C, the values of the prefactors deduced from our simulations and $\Sigma=0.9$, one finds δ_c

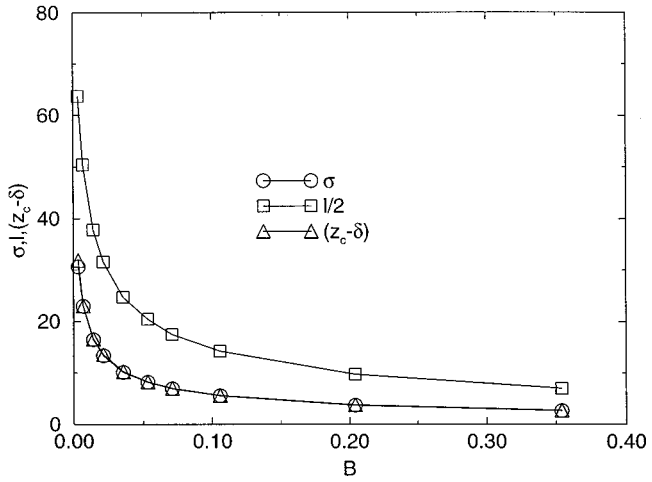

FIG. 11. Stationary case. Evolution of the equivalent smooth line as a function of the Bond number. Each symbol corresponds to the average over 50 realizations. These results were obtained with square lattices of size 400×400.

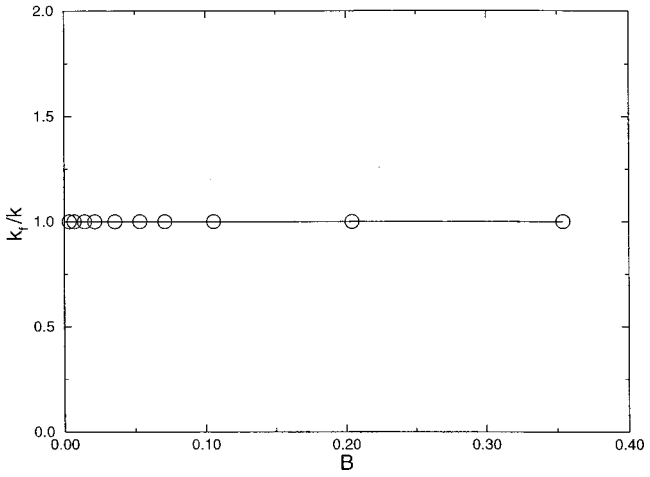

FIG. 12. Stationary case. Front global permeability k_f as a function of the Bond number. k is the permeability of the network. Each symbol corresponds to the average over 50 realizations. These results were obtained with square lattices of size 400×400.

$\approx 60\,000$ (in lattice units), i.e., $\delta_c \approx 600$ mm. This corresponds to $z_c \approx 666$ mm and $l \approx 90$ mm, whereas, when the front forms, z_c and l are of the order of a few tens of lattice unit, i.e., $O(0.1\,\text{mm})$. This case corresponds to the portion of the curves in Fig. 6 where $(z_c-\delta)/(z_c-\delta)_{\min}$ varies quickly. Also in this case, the third term on the left-hand side of Eq. (22) is not small compared to the first one. This can lead, therefore, to nontrivial behavior, i.e., drying rates not scaling as $1/\sqrt{t}$.

B. Stationary case

In this section, we consider a situation where the drying front reaches a stationary position. This can be obtained when the evaporation flux is exactly balanced by the liquid flow feeding the porous medium. This type of situation is sketched in Fig. 10. For a given system (porous medium plus fluids plus external transfer conditions), the pressure in the liquid at the entrance of the porous medium must be in a certain range for the front to reach a stationary position within the porous domain. As for the transient cases, the occurrence of the steady evaporation regime depends on the interplay between the gravity, viscous, and capillary forces. In what follows, we consider the case where the gravity forces can be ignored and, therefore, where the process is controlled by only the capillary and viscous forces. This is *a priori* the most interesting case because of the dependence of the overall front thickness with the capillary number, i.e., in fact with the entrance pressure. Since we are only interested in a stationary front, we assumed that all disconnected clusters have disappeared when the stationary regime is reached. This is what is expected within the framework of the assumptions of the present work (see Sec. I), since there is no feeding mechanism of a disconnected cluster that could balance the evaporation flux at the boundary of such a cluster. This is in fact directly associated with the assumption of negligible liquid film flows.

Similarly to the transient case, we define the front global mass transfer coefficient Y by

$$\Phi = Y c_e = \rho_v D^* b W \frac{c_e}{\delta}, \tag{23}$$

where δ is the position of the smooth line at uniform concentration c_e leading to the same concentration field in the far field as for the drying front. From the consideration of a somewhat analogous problem in Refs. [22] and [23], one expects

$$(z_c-\delta) \approx \sigma. \tag{24}$$

This result was confirmed by numerical simulation as depicted in Fig. 11. The results shown in Fig. 11 were obtained for 400×400 networks. Fifty realizations for ten different values of the Bond number were considered. It should be noted here that the stationary case is much less demanding in terms of computation. Each front is in fact generated by the invasion percolation algorithm (including gravity effects). Then the disconnected clusters are removed, and the vapor concentration distribution is computed. In contrast with the transient case, that requires the computation of the vapor concentration field after each invasion, only one computation of this field is performed in the stationary case. This makes it possible to consider large networks.

When the front reaches its stationary position, the flow rate Q through the liquid zone is equal to the evaporation flux,

$$Q = \rho_l v_D W b = \Phi, \tag{25}$$

where v_D is the filtration velocity. Making use of Darcy's law, the pressure variation in the liquid zone can be expressed as

$$P_e = P_l(z_{\max}) + \frac{\mu_L v_D}{k}[L-(l+z_{\min})], \tag{26}$$

where k is the permeability. The pressure variation within the front between $z_{\max}$ and z_c can be expressed as

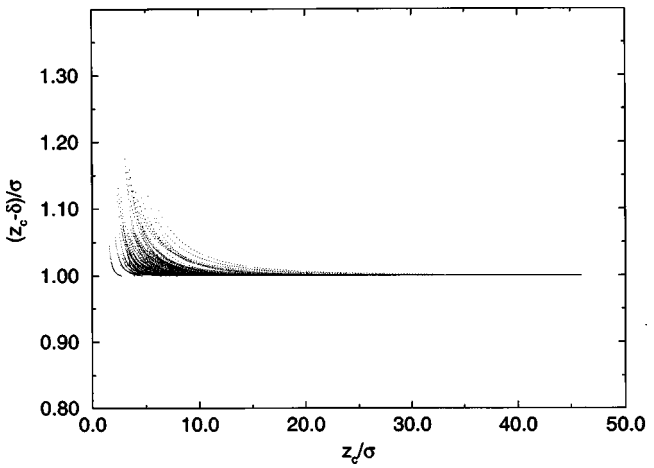

FIG. 13. Stationary case. Evolution of $z_c-\delta$ as a function of z_c. The results of ten realizations are plotted (ten different values of the Bond number were considered for each realization). $z_c-\delta$ reaches its established value when z_c is about equal to 20σ. These results were obtained with square lattices of size 200×200.

$$P_l(z_{\max})-P_l(z_c)=\frac{\mu_L v_D l}{2k_f}, \tag{27}$$

where k_f is the global front permeability between z_c and $z_{\max}$. As the liquid phase distribution is compact, one expects that k_f is not very different from k. As shown in Fig. 12, the numerical simulations indicate that

$$k_f=k. \tag{28}$$

The pressure in the liquid at z_c can be related to the capillary pressure P_c at z_c. For uniform bond size distributions between $r_{\min}$ and $r_{\max}$, we can express P_c at z_c as

$$P_c(z_c)=P_g-P_l(z_c)=\frac{2\gamma}{r_c}, \tag{29}$$

where r_c is given by $p_c=[(r_{\max}-r_c)/\Sigma]$ in which p_c is the percolation threshold of network.

Combining the above equations leads to

$$L-\sigma=v_D^{-1}\left[\rho_v D^* c_e+\rho_e\frac{k}{\mu_L}(P_e-P_g+P_c)\right], \tag{30}$$

which shows that the filtration velocity, i.e., the evaporation flux, is a nonlinear function of the pressure difference $\Delta P=P_e-P_g$, since there is a power dependence between σ and $v_D[\sigma\propto(\mathrm{Ca}/\Sigma)^{-\nu/(1+\nu)}]$. Naturally, this nontrivial behavior is obtained provided that σ is not too small compared to L. As shown in Fig. 13, Eq. (24) holds for $z_c\geqslant20\sigma$, i.e., $\delta\geqslant19\sigma$. 200×200 networks were used for obtaining the results depicted in Fig. 13. Therefore, we conclude that σ is in fact necessarily small compared to L when Eq. (30) is valid. As a result, nontrivial behaviors can be expected essentially for the nonestablished regime, i.e., before $z_c-\delta$ reaches its asymptotic value σ. For given fluids, geometry, and gas pressure P_g, one can also determine the entrance pressure range $[P_{\mathrm{emin}},P_{\mathrm{emax}}]$ for which a front will be observed within the porous domain, and Eq. (30) is valid. Thus, P_{emin} corresponds to the position of the smooth equivalent line $\delta_{\min}$ given by the equation

$$\delta_{\min}=19j\left(\frac{\rho_v D^* c_e\mu_L}{\rho_L\gamma\Sigma\,\delta_{\min}}\right)^{-\nu/(1+\nu)}, \tag{31}$$

where j is the numerical prefactor in the scaling of σ, i.e., $\sigma=j(\mathrm{Ca}/\Sigma)^{-\nu/(1+\nu)}$. Once $\delta_{\min}$ is determined, P_{emin} is easily determined by combining Eqs. (23), (25), and (30). To determine P_{emax}, one must first determine how far from the exit should the front be located for Eq. (28) to hold. The simulations indicate that Eq. (28) holds until the front reaches the exit, i.e., $z_c=L-l/2$, i.e., $\delta_{\max}=L-l/2-\sigma$. $\delta_{\max}$ can then be determined by an equation similar to Eq. (31). Once $\delta_{\max}$ is determined, P_{emax} can be determined in a similar manner as P_{emin}.

V. DISCUSSION

A. Influence of pressure gradient variation in the liquid

As mentioned in Sec. IV A, the scaling in terms of the capillary number is based on the assumption that the pressure gradient is constant across the width of the front, in direct analogy with the situations where the pressure gradient is induced by the gravity forces. We made an attempt to explore the influence of possible pressure gradient variations across the front width when the gradients are induced by the viscous forces. To this end, we performed a series of pore network simulations including the computation of the pressure fields in the liquid. The results can be found in Ref. [24], and are not reported here. We found that the pressure gradient is indeed not constant. It tends to be greater in the region of the front located closer to the dry zone. We also explored the scaling of σ and l in terms of the capillary numbers. A correction to scaling was found for l and σ. The exponents -0.55 for l and 0.59 for σ drawn from the simulations are slightly greater than the exponent -0.52 and -0.57 corresponding to a constant pressure gradient. These simulations were performed over 400×400 networks. This issue would deserve to be explored further.

B. Phase distribution in two dimensions (transient case)

In two dimensions we can make use of the scaling for l in order to delineate the various patterns discussed in Sec. II. According to the results presented in this paper, we have

$$\frac{L_g}{a}\propto B^{-0.52} \tag{32}$$

and

$$\frac{L_{cap}}{a}\propto \mathrm{Ca}^{*(-0.52/0.77)}, \tag{33}$$

with $\mathrm{Ca}^*=e\mu_L/\gamma\rho_L$, where e is the evaporation flux density. On the basis of Eqs. (32) and (33), it is straightforward to adapt the considerations of Sec. II.

VI. SUMMARY AND CONCLUSIONS

In this paper, a model of 2D drying in the presence of a stabilized front has been studied numerically by means of pore network simulations. The width of the front can be characterized by the mean perpendicular distance between the most advanced and least advanced points of the front. We have shown that this width (l) scales in two dimensions as $l \propto B^{-1+(1+\beta)/(1+\nu)}$, where β is the percolation probability exponent, and ν is the correlation length exponent, when gravity stabilizes the front. It is worth noting that this scaling relation is of interest not only for the specific drying problem considered in this paper but also for other situations that can be analyzed in terms of percolation in a gradient (diffusion front, etc.). This scaling is in a good agreement with the experimental result of Shaw [6].

The global mass transfer coefficient of the front was quantified for transient situations as well as for situations where the front reaches a stationary position within the porous domain. It was found that the global mass transfer coefficient, characterized by means of the position of the equivalent smooth line at constant concentration, follows a power law dependence with the Bond number, i.e., the percolation probability gradient. In the stationary case, we found that the location of the equivalent smooth line is $z_c - \sigma$, where z_c is the average position of the front and σ is the standard deviation of the front point positions. In the transient case, the position $z_c - \delta$ of the equivalent line was found to be located between $z_c - \sigma$ and $z_c - l/2$, and to scale as $B^{-0.63}$. In the transient case, it was also obtained that the fraction f of the evaporation flux corresponding to the contribution of the main cluster was scale dependent, $f \propto B^{-0.23}$. These results are valid for the established regimes, i.e., when the front is located sufficiently away from the surface of the porous medium.

These results were applied to the viscous case, i.e., we assumed that the pressure gradients induced by the viscous effects are constant across the front. It was found that nontrivial behaviors could be expected, i.e., drying rates not scaling as $1/\sqrt{t}$ in the transient case, and nonlinear relations between the pressure difference and the evaporation flux in the stationary case. However these nontrivial behaviors are essentially expected for the nonestablished regimes, i.e., before scaling equations (14) and (17) hold. Although preliminary results indicate that the assumption of a constant pressure gradient across the front seems to be satisfactory, further work is needed to completely explore this issue.

In the present effort, film flows were neglected. It would be interesting to reconsider the problem in the presence of film flows and also in three dimensions (an insight into drying in 3D geometries can be found in Ref. [25], and in the recent paper by Tsimpanogiannis *et al.* [26], where a discussion on the viscous effects and a continuum description for the regime upstream of the front was also presented).

ACKNOWLEDGMENT

The authors are grateful to J. Georgiadis for a careful reading of the manuscript.

[1] G. W. Scherer, J. Am. Ceram. Soc. **73**, 3 (1990).
[2] S. Whitaker, *Advances in Heat Transfer* (Academic, New York, 1977), Vol. 13.
[3] O. Krisher, *Die Wissenshaftlichen Grundlagen der Trocknungstecknick* (Springer, Berlin, 1963), Vol. 1, p. 298.
[4] A. V. Luikov, *Heat and Mass Transfer in Capillary Porous Bodies* (Pergamon, Oxford, 1966).
[5] N. H. Ceaglske and O. A. Hougen, Ind. Eng. Chem. **29**, 805 (1937).
[6] T. M. Shaw, Phys. Rev. Lett. **59**, 1671 (1987).
[7] M. Prat, Int. J. Multiphase Flow **21**, 875 (1995).
[8] J. B. Laurindo and M. Prat, Chem. Eng. Sci. **51**, 5171 (1996).
[9] M. Sahimi, *Flow and Transport in Porous Media and Fractured Rock* (VCH, Weinheim, 1995).
[10] R. Lenormand and S. Bories, C. R. Hebd. Seances Acad. Sci., Ser. B **291**, 279 (1980); D. Wilkinson and J. F. Willemsen, J. Phys. A **16**, 3365 (1983).
[11] Y. C. Yortsos, B. Xu, and D. Salin, Phys. Rev. Lett. **79**, 4581 (1997); B. Xu, Y. C. Yortsos, and D. Salin, Phys. Rev. E **57**, 1 (1998); **57**, 739 (1998).
[12] J. P. Hulin, E. Clement, C. Baudet, J. F. Gouyet, and M. Rosso, Phys. Rev. Lett. **61**, 333 (1988).
[13] J. F. Gouyet, M. Rosso, and B. Sapoval, Phys. Rev. B **37**, 1832 (1988).
[14] A. Birovljev, L. Furuberg, J. Feder, T. Jossang, K. J. Maloy, and A. Aharony, Phys. Rev. Lett. **67**, 584 (1991).
[15] D. S. Freitas and M. Prat (unpublished); F. Plourde and M. Prat (unpublished).
[16] V. Frette, J. Feder, T. Jossang, and P. Meakin, Phys. Rev. Lett. **68**, 21 (1992); **68**, 3164 (1992).
[17] J. B. Laurindo and M. Prat, Chem. Eng. Sci. **53**, 2257 (1998).
[18] D. Wilkinson, Phys. Rev. A **30**, 520 (1984).
[19] B. Sapoval, M. Rosso, and J. F. Gouyet, J. Phys. (France) Lett. **46**, 149 (1985).
[20] D. Vandembroucq and S. Roux, Phys. Rev. E **55**, 6171 (1997).
[21] R. Lenormand, E. Touboul, and C. Zarcone, J. Fluid Mech. **189**, 165 (1988).
[22] M. E. Cates and T. A. Witten, Phys. Rev. A **35**, 1809 (1988).
[23] C. Satik, X. Li, and Y. C. Yortsos, Phys. Rev. E **51**, 4 (1995); **51**, 3286 (1995).
[24] F. Bouleux, Ph.D. thesis, Institut National Polytechnique de Toulouse, France, 1999 (unpublished).
[25] Y. Le Bray and M. Prat, Int. J. Heat Mass Transf. **42**, 4207 (1999).
[26] I. N. Tsimpanogiannis, Y. C. Yortsos, S. Poulou, N. Kanellopoulos, and A. K. Stubos, Phys. Rev. E **59**, 4353 (1999).